

Mechanism of Bismuth Telluride Exfoliation in an Ionic Liquid Solvent

Thomas Ludwig,[†] Lingling Guo,^{†,‡} Parker McCrary,[§] Zhongtao Zhang,[†] Haley Gordon,^{⊥,#} Haiyu Quan,^{†,‡} Michael Stanton,[▽] Rachel M. Frazier,^{||} Robin D. Rogers,[§] Hung-Ta Wang,^{†,‡} and C. Heath Turner^{*,†}

[†]Department of Chemical and Biological Engineering, [‡]Center for Materials for Information Technology, [§]Department of Chemistry, and ^{||}Alabama Innovation and Mentoring of Entrepreneurs, The University of Alabama, Tuscaloosa, Alabama 35487, United States

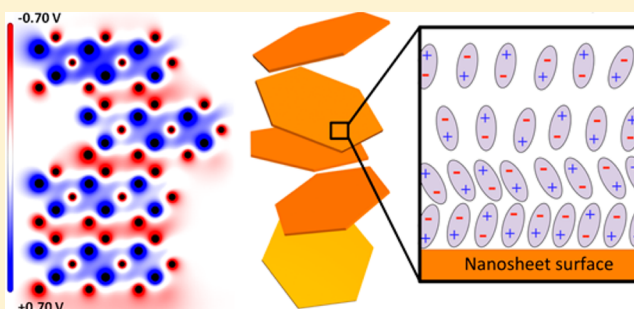
[⊥]Department of Chemical and Biomolecular Engineering, University of Notre Dame, Notre Dame, Indiana 46556, United States

[#]St. Mary's College, Notre Dame, Indiana 46556, United States

[▽]Department of Materials Science and Engineering, University of Pennsylvania, Philadelphia, Pennsylvania 19104, United States

Supporting Information

ABSTRACT: Bismuth telluride (Bi_2Te_3) is a well-known thermoelectric material that has a layered crystal structure. Exfoliating Bi_2Te_3 to produce two-dimensional (2D) nanosheets is extremely important because the exfoliated nanosheets possess unique properties, which can potentially revolutionize several material technologies such as thermoelectrics, heterogeneous catalysts, and infrared detectors. In this work, ionic liquid (IL) 1-butyl-3-methylimidazolium chloride ($[\text{C}_4\text{mim}]\text{Cl}$) is used to exfoliate Bi_2Te_3 nanoplatelets. In both experiments and in molecular dynamics (MD) simulations, the Bi_2Te_3 nanoplatelets yield a stable dispersion of 2D nanosheets in the IL solvent, and our MD simulations provide molecular-level insight into the kinetics and thermodynamics of the exfoliation process. An analysis of the dynamics of Bi_2Te_3 during exfoliation indicates that the relative translation (sliding apart) of adjacent layers caused by IL-induced forces plays an important role in the process. Moreover, an evaluation of the MD trajectories and electrostatic interactions indicates that the $[\text{C}_4\text{mim}]^+$ cation is primarily responsible for initiating Bi_2Te_3 layer sliding and separation, while the Cl^- anion is less active. Overall, our combined experimental and computational investigation highlights the effectiveness of IL-assisted exfoliation, and the underlying molecular-level insights should accelerate the development of future exfoliation techniques for producing 2D chalcogenide materials.



1. INTRODUCTION

Bulk bismuth telluride (Bi_2Te_3) and other V–VI group chalcogenide materials have been widely used in thermoelectric applications since the 1950s. Recently, nontrivial topological surface states were discovered on the surfaces of these V–VI group chalcogenides.^{1,2} Because the topological surface states are unaffected by impurity defects and structural defects, the charge transport on the Bi_2Te_3 surface is essentially dissipationless, providing promising electrical, thermal, and chemical properties. To utilize the unique charge transport, it is important to manufacture two-dimensional (2D) nanosheets that can enhance the surface charges and simultaneously suppress ordinary bulk charges. More specifically, the charge transport in a Bi_2Te_3 2D nanosheet with a thickness of less than 10 nm should be dominated by the topological surface states.^{3,4} The band gap of topological surface states could be formed by reducing the 2D nanosheet thickness to less than 5 nm (i.e., the penetration depth of topological surface states in Bi_2Te_3); consequently, the physical and chemical properties can be entirely different from those of thicker sheets. Therefore, there is a need to develop a scalable, inexpensive, and environ-

mentally friendly process that can produce Bi_2Te_3 2D nanosheets with a uniform thickness.

Bi_2Te_3 2D nanosheets have been found to be randomly produced among other products of vapor-phase depositions^{5,6} or liquid-phase syntheses.^{7,8} Liquid-phase syntheses are relatively facile, inexpensive, and would seem to be a more suitable route for large-scale production. However, separating 2D nanosheets from thick nanoplatelets is a formidable task. Instead, solvent-assisted exfoliation could be used to transform a heterogeneous mixture of thick microflakes of layered materials into a homogeneous dispersion of uniform 2D nanosheets similar to graphene,⁹ boron nitrides,¹⁰ and other transition-metal dichalcogenides. In the Bi_2Te_3 crystal, five covalently bonded atomic layers in the order of $\text{Te}_{(1)}\text{-Bi-Te}_{(2)}\text{-Bi-Te}_{(1)}$ form a 1-nm-thick charge-neutral quintuple sheet, and the bonding between adjacent quintuple sheets is a much weaker van der Waals interaction.¹¹ Analogous to the

Received: January 20, 2015

Revised: March 5, 2015

Published: March 11, 2015

exfoliation of graphite to produce graphene nanosheets, Bi_2Te_3 2D nanosheets of Bi_2Te_3 can be produced by breaking the weak interlayer bonding between adjacent quintuple sheets.

Various methods for exfoliating Bi_2Te_3 have been reported, but solvent-assisted exfoliation by ionic liquid (IL) exfoliants is of particular interest for several reasons. Room-temperature ILs, organic salts with melting points below 100 °C, are attractive exfoliants¹² due to their superior chemical and physical properties (e.g., low vapor pressure, high thermal stability, tunable viscosity, and high ionic conductivity) as well as the potential for solvent recyclability.^{13–19} Currently, the molecular-level behavior of Bi_2Te_3 in an IL solvent has not been well characterized, but this fundamental information would potentially enable the development of optimal exfoliation solvents and scalable manufacturing processes. Molecular dynamics (MD) simulations have been widely used to simulate interfacial interactions as well as the general thermophysical properties of ILs,^{20,21} so this simulation approach is well suited to our current system of interest.

There are some recent simulation reports in the literature from Kamath and Baker of bilayer graphene²² and bilayer hexagonal boron nitride (h-BN)²³ exfoliation within an ionic liquid solvent. The same force field is used for the $[\text{C}_4\text{mim}]^+$ cation, but the current study focuses on Bi_2Te_3 materials, which are both chemically and structurally distinct from these previous systems. Our simulation goals and techniques are also different. Hexagonal boron nitride and graphene are isoelectronic, they have similar hexagonal lattice structures, and their surface energies are similar (h-BN of about 50 mJ/m² and graphene of about 47 mJ/m²).^{24,25} The thicker quintuple layers of Bi_2Te_3 , although net charge-neutral, are terminated with negatively charged Te atoms in the basal plane, resulting in a negatively charged surface. Kamath and Baker use adaptive bias force (ABF) MD simulation methods, making use of an external biasing force to facilitate adequate sampling of the reaction coordinate to calculate the free-energy difference in solvation. These studies used an initial configuration of two parallel monolayer sheets separated by 10 Å, equilibrated so that IL molecules filled the interlayer space in the initial configuration. Then, ABF simulations were used to transfer one of the monolayers from the IL phase into a vacuum. Because the layers are already separated by IL molecules in the initial configuration, the initial exfoliation was not directly observable. In contrast, the current study aims to study the initial exfoliation mechanism and dynamics. Thus, the initial configuration of Bi_2Te_3 in our study coincides with the interlayer spacing of the bulk-phase material.

In this work, the exfoliation of Bi_2Te_3 by IL 1-butyl-3-methylimidazolium chloride, $[\text{C}_4\text{mim}]\text{Cl}$, is successfully demonstrated using both experimental and simulation approaches. In our simulations, the exfoliation and dispersion processes occurred rapidly, and no artificial pulling or steered dynamics were required to achieve separation. The MD simulations are used to quantify the solvation structure and to investigate the exfoliation mechanism. Further analysis of the MD trajectories and electrostatic interactions indicates that the $[\text{C}_4\text{mim}]^+$ species is primarily involved in the initiation of the Bi_2Te_3 layer separation, followed by the development of well-defined IL surface layers. The analysis of the thermodynamic and kinetic features of this system should accelerate the development of future exfoliation techniques for producing 2D chalcogenide materials.

2. EXPERIMENTAL METHODS

2.1. Bi_2Te_3 Nanoplatelet Synthesis. Bi_2Te_3 nanoplatelets were synthesized using the solvothermal reaction, and then they were used in the IL-assisted exfoliation. The procedure for synthesizing Bi_2Te_3 nanoplatelets is briefly described in the following text. The precursors of Bi_2O_3 , TeO_2 , and NaOH powders were dissolved in ethylene glycol, followed by the addition of poly(vinylpyrrolidone) (PVP). All chemicals were purchased from Alfa Aesar, and they were used without any pretreatment. The solvothermal reaction occurred in an autoclave (Parr) at 200–250 °C for 10–24 h. The nanoplatelet products were washed with several cycles of solvents, 1-methyl-2-pyrrolidinone and water, and then they were dried in deionized water before exfoliation. The as-synthesized and washed Bi_2Te_3 nanoplatelets were characterized by scanning electron microscopy (SEM, JEOL 7000 FE), energy dispersive spectroscopy (EDX, Oxford instrument equipped with a JEOL 7000 FE), and X-ray diffraction (Bruker D8). Additional details of the syntheses can be found elsewhere.^{26,27}

2.2. $[\text{C}_4\text{mim}]\text{Cl}$ Synthesis. 1-Methylimidazole (146 mL, 1.8 mol) was placed into a 1 L round-bottomed flask equipped with a Teflon stir bar and a condenser. Then, acetonitrile (220 mL) was added, followed by 1-chlorobutane (190 mL, 1.8 mol), and the solution was heated under reflux for 72 h. After 72 h, acetonitrile was removed using a rotary evaporator under vacuum. The residue was dissolved in a minimal amount of dichloromethane and precipitated with toluene at –78 °C (acetone/dry ice). White crystals of the product were isolated by filtration, washed with cold toluene, and dried under vacuum. Yield: 124.5 g (78%). ¹H NMR (250 MHz, CDCl_3): 10.79 (s, 1H), 7.50 (d, 1H), 7.37 (d, 1H), 4.30 (t, 2H), 4.10 (s, 3H), 1.87 (quin, 4H), 1.34 (sext, 2H), 0.93 (t, 3H). ¹³C{¹H} NMR (74.5 MHz, CDCl_3): 137.06, 123.53, 122.00, 48.53, 35.40, 31.48, 19.41, 13.27.

2.3. IL-Assisted Exfoliation. In a batch, 0.05 wt % of rinsed Bi_2Te_3 nanoplatelets in $[\text{C}_4\text{mim}]\text{Cl}$ was tip sonicated at a power of 225–600 W (Sonics, VCX-750) for 1 h at a temperature of 80–150 °C. UV–vis absorption (Shimadzu UV-1800 UV), XRD, and atomic force microscopy (AFM, Park XE 70) were used to characterize the dispersion and the exfoliated 2D nanosheets. Tapping-mode AFM with a hard cantilever (PPP-NCHR from Park) was used specifically for analyzing the nanoplatelet/nanosheet thicknesses, before and after exfoliation.

3. SIMULATION METHODOLOGY AND MODEL

The molecular dynamics (MD) simulations were performed using GROMACS 4.6.4 molecular dynamics software.²⁸ The OPLS-AA force field²⁹ was used to describe the molecular interactions in the system, and periodic boundary conditions were applied in all three spatial dimensions. For short-range nonbonded interactions (in the IL as well as between the IL and Bi_2Te_3), the Lennard-Jones potential was used, and partial charges on the atoms were used to account for the electrostatic interactions, according to

$$U_{ij}(r_{ij}) = 4\epsilon_{ij} \left[\left(\frac{\sigma_{ij}}{r_{ij}} \right)^{12} - \left(\frac{\sigma_{ij}}{r_{ij}} \right)^6 \right] + \frac{q_i q_j}{r_{ij}} \quad (1)$$

In eq 1, σ is the diameter, ϵ is the well depth, r is the separation distance between interaction sites, and q represents the partial charge on each site. The Lennard-Jones interaction cutoff distance was set at 1.4 nm. For long-range nonbonded electrostatic interactions, the smooth particle mesh Ewald sum (SPME) was used,³⁰ with a real-space cutoff of 1.4 nm and a reciprocal-space parameter of 0.16 nm. We have used this general simulation approach to model other IL and imidazole-based compounds, achieving excellent agreement with many experimental thermophysical properties.^{31–33}

The intramolecular force field (describing the interactions within the quintuple sheets) for Bi_2Te_3 in this work was taken from the two-body interatomic Morse potential form developed by Qiu and Ruan,³⁴ but it should be mentioned that another similar force field (also based on the Morse potential) has been developed by Huang and Kavany.³⁵ The parameters for the Qiu and Ruan force field (used here) were developed by using first-principles density-functional theory and fitting to experimental elastic and phonon data. This potential was then tested by simulating the thermal conductivity, elastic properties, and phonon properties of the Bi_2Te_3 crystal with MD simulations.³⁴ These parameters have previously been implemented in different simulation studies to model several systems, such as an MD study of a quintuple film,³⁶ a Bi_2Te_3 wire model,³⁷ and ultrafast laser-induced nonthermal melting of Bi_2Te_3 .³⁸ The Bi_2Te_3 potential (U_M) consists of a short-range Morse potential plus partial charge sites

$$U_M(r_{ij}) = D_e \left[\left\{ 1 - e^{-a(r_{ij}-r_0)} \right\}^2 - 1 \right] + \frac{q_i q_j}{r_{ij}} \quad (2)$$

with U_M representing the Morse pair potential, supplemented with electrostatic interactions. Coefficient D_e is the potential well depth, r_0 is the equilibrium bond distance, and a is the coefficient of bond elasticity. The partial charges for the atomic sites included in this force field were developed by Kullmann et al.³⁹

The Lennard-Jones parameters of Bi and Te atoms describing the van der Waals interactions with the IL solvent molecules and between neighboring Bi_2Te_3 quintuple sheets were adopted from the universal force field (UFF),⁴⁰ a broadly applicable force field covering the full periodic table for MD simulations. The cross-term interactions between the IL ions and the Bi_2Te_3 atoms (as well as Bi–Te interactions between quintuple sheets) were approximated by the standard Lorentz–Berthelot mixing rules: $\sigma_{ij} = 0.5(\sigma_i + \sigma_j)$ and $\epsilon_{ij} = (\epsilon_i \epsilon_j)^{0.5}$. The force field for the IL–IL interactions was implemented using parameters developed by Lopes et al.²⁰ (Supporting Information, Tables S-1 and S-2 and Figures S-3 and S-4). Fixed bond-length constraints for C–H bonds were imposed using the LINCS algorithm to accelerate the simulations, which should result in a negligible loss of accuracy. All molecular dynamics simulations in this study were propagated through time using the leapfrog integrator, with a time step of 0.001 ps. Production-phase simulations were carried out in the isothermal–isobaric (NPT) ensemble. In the NPT ensemble, the pressure was maintained with the Parrinello–Rahman barostat at a pressure of 1 bar,^{41,42} and the temperature was maintained using the Nose–Hoover thermostat.⁴³

The initial preparation of our computational model of Bi_2Te_3 dissolved in $[\text{C}_4\text{mim}]\text{Cl}$ involved two steps. The first step involved separately equilibrating a simulation box of $[\text{C}_4\text{mim}]\text{Cl}$ in the NPT ensemble and equilibrating a configuration of Bi_2Te_3 in the canonical (NVT) ensemble. The initial configuration of Bi_2Te_3 was generated using lattice parameters reported from crystallographic data,⁴⁴ from which a single quintuple-layer hexagonal nanosheet of Bi_2Te_3 was cut. This nanosheet, lying in the xy plane, was copied and repeatedly shifted in the z direction normal to the xy plane to form a four-layer stack of identical quintuple sheets. A hexagonal cross section was chosen because this is the dominant shape seen in experimental studies.^{45,46} Each hexagonal quintuple layer had an approximate cross-sectional area of 379 \AA^2 , 100 atoms total,

a Bi/Te ratio of 2:3, and a net zero electrostatic charge. The Bi_2Te_3 system was equilibrated in the NVT ensemble (in vacuum) for 100 ps at 298 K in a simulation box of $6 \times 6 \times 12 \text{ nm}^3$. Position restraints were placed on a single layer of atoms to prevent any net translational or rotational motion of the Bi_2Te_3 model. During equilibration, the hexagonal c axis of our model is found to be approximately 3.276 nm, which is 8% larger than the experimental value (3.034 nm).⁴⁷ The difference is attributed to the UFF σ value describing interfacial Te, which leads to a slight expansion.

In initial benchmarking (in vacuum at 0 K), we determined the dependence of surface energy on both the total number of Bi_2Te_3 layers and on the cross-sectional area of the model. The surface energy of Bi_2Te_3 in vacuum was estimated by calculating the energy needed to introduce a vacuum layer within a bulk Bi_2Te_3 stack of hexagonal sheets (normalized by the cross-sectional area). The intermolecular force field between the Bi_2Te_3 layers was consistent with the MD simulations in the IL solvent, and the intramolecular structure of the Bi_2Te_3 quintuple sheets was kept rigid. The results are presented in Table 1 below, and additional calculation details are provided in the Supporting Information.

Table 1. Dependence of Surface Energy on the Cross-Sectional Area of the Bi_2Te_3 Model

cross-sectional area (\AA^2)	surface energy (mJ/m^2)
379	63.2
628	70.3
1549	81.1

The surface energy is found to increase by approximately 28% as the cross-sectional area increases by 4-fold. Although the largest Bi_2Te_3 model would be preferable, the 379 \AA^2 model should provide a reasonable approximation of the exfoliation process and representative mechanistic insights, with a moderate compromise in quantitative accuracy. The largest model would require a significant increase in the system size (number of ionic liquid molecules) beyond the limits of our current computational resources, especially considering the long simulation times needed to acquire accurate statistics.

The surface energy is found to be essentially independent of the total number of quintuple layers in the configuration as long as at least four quintuple layers are used. For instance, a model with 12 quintuple layers versus 4 quintuple layers was found to change the calculated surface energy by less than 1%. Overall, these results motivated our choice of the Bi_2Te_3 model size (four-layer quintuple stack with a 379 \AA^2 cross section), which represents a reasonable balance between accuracy and computational demands. Although the Bi_2Te_3 structures in our experiments are significantly larger, our model is expected to be representative of the interfacial phenomena associated with the larger systems.

A comparison of these Bi_2Te_3 surface energy values to experimental and simulated values for similar layered materials, such as graphene and graphene oxide, reveals that these surface energy values are very similar.²⁵ The Bi_2Te_3 force field was originally developed for use in lattice dynamics, so the quantitative accuracy of this force field for modeling solid–liquid interfaces improves with additional refinement by benchmarking against experimental adsorption data. In general, the interactions between molecular liquids and chalcogenides are not very well characterized, especially from the standpoint

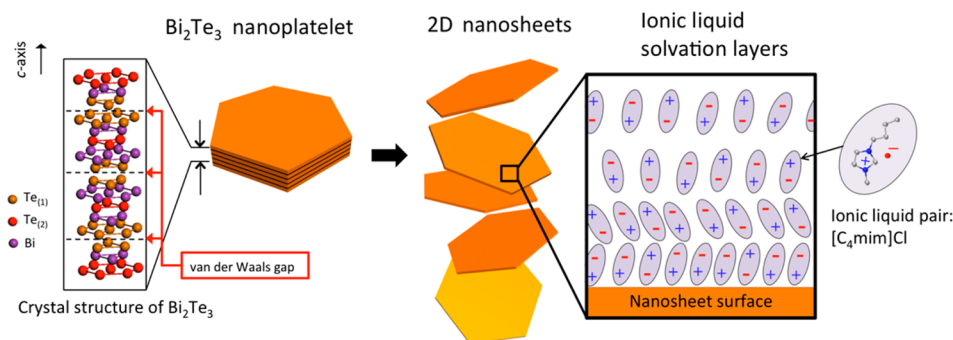


Figure 1. Schematic of the IL exfoliation process for generating 2D nanosheets. The Bi_2Te_3 crystal structure is shown on the left, and an illustration of the IL solvation layers is shown on the right.

of intermolecular potential models, which can vary greatly.^{48,49} To the best of our knowledge, no direct experimental measurement of the surface energy has been reported for Bi_2Te_3 .

The $[\text{C}_4\text{mim}]\text{Cl}$ solvent was separately equilibrated in the NPT ensemble in a similarly sized simulation box, with a total of 2000 $[\text{C}_4\text{mim}]\text{Cl}$ ion pairs. A total of 6 ns of equilibration was performed by heating the system to 400 K, followed by a quench to 380 K. The higher temperatures helped the system efficiently sample phase space while staying well above the melting point of $[\text{C}_4\text{mim}]\text{Cl}$ (approximately 314–339 K).^{50,51} From the resulting equilibrated configuration, a cylindrical volume roughly corresponding to the size of the Bi_2Te_3 system was deleted from the IL solvent (to make room for the Bi_2Te_3 insertion). The Bi_2Te_3 model was then placed into this empty volume, surrounded by the remaining 1868 ion pairs. This was followed by more equilibration in the NPT ensemble, prior to the production phase. Position restraints were placed on all of the Bi_2Te_3 layers during the combined equilibration stage (IL + Bi_2Te_3) in order to hold the layers together as the surrounding IL relaxed, thus preventing premature exfoliation or layer separation. Once the combined equilibration stage was complete, the position restraints were removed.

To gather temperature-dependent exfoliation kinetics data, production simulations were performed in the NPT ensemble at seven distinct temperatures over the temperature interval from 350 to 650 K (with 50 K increments) while the pressure was held at 1 bar. The lower limit of 350 K was chosen to ensure liquid behavior, as the melting point has been reported to fall in the range of 314 to 339 K.^{50,51} The upper limit of 650 K was chosen because higher temperatures allow for a more complete sampling of the exfoliation process, which proceeds more rapidly and to a greater extent at higher temperatures. However, it should be noted that experiments indicate that the onset of thermal decomposition for $[\text{C}_4\text{mim}]\text{Cl}$ is between 527⁵¹ and 537 K.⁵² The higher-temperature limit also allows a more thorough understanding of thermal effects on the process. Thus, the experimentally useful temperature range of $[\text{C}_4\text{mim}]\text{Cl}$ likely corresponds to the lower region of our chosen temperature range. Four independent replicate simulations were run at each temperature to gather representative statistics. For each simulation, the initial configuration of the stacked Bi_2Te_3 structure was restrained while the surrounding IL was equilibrated. After system equilibration, the production runs were conducted with the bottom-most Bi_2Te_3 quintuple sheet kept restrained while the rest of the layers were unrestrained. The simulations were propagated through time until obvious

exfoliation effects were observed (based on an evaluation of the exposed surface area).

4. RESULTS AND ANALYSIS

4.1. Experimental Exfoliation of Bi_2Te_3 . Figure 1 shows a schematic of the exfoliation process presented in this work. In Figure 2, the elemental composition and the rhombohedral

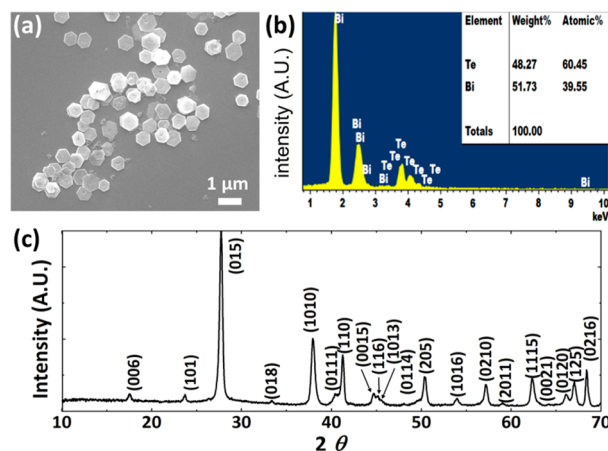


Figure 2. (a) SEM image of the Bi_2Te_3 nanoplatelets dispersed on the silicon substrate. (b) EDS spectrum providing the atomic compositions of Bi and Te to be 39.55 and 60.45%, respectively. (c) XRD pattern of the Bi_2Te_3 nanoplatelets. All peaks are indexed with the rhombohedral Bi_2Te_3 crystal (PDF card no. 15-0863).

crystal structure of the solvothermal reaction product were used to confirm the presence of crystallized Bi_2Te_3 nanoplatelets. These Bi_2Te_3 nanoplatelets were the raw materials used in the ionic-liquid-assisted exfoliation. Figure 3 provides a compilation of the actual exfoliation data. During the sonication process, the color of the $\text{Bi}_2\text{Te}_3/\text{IL}$ solution became progressively darker, which is consistent with the increased UV–vis absorbance spectra, shown in Figure 3a. As a homogeneous dispersion of the nanosheets gradually formed, the light scattering became more prominent than the absorption, and this intensified the overall signal. After the 20 min sonication, the UV–vis overall intensity had greatly increased (as compared to that of the $\text{Bi}_2\text{Te}_3/\text{water}$ solution) and even reached the saturation of the detector. Interestingly, the peak of UV–vis absorbance at ~ 330 nm is shown and highlighted in Figure 3b. The control experiment confirmed that there was no absorption at 330 nm for the pure $[\text{C}_4\text{mim}]\text{Cl}$ solvent, before and after the same degree of tip sonication (available in the Supporting

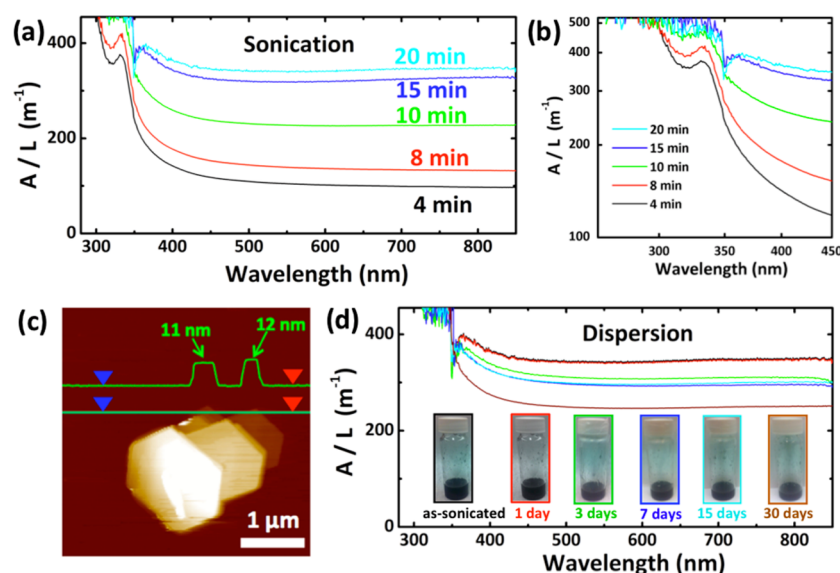


Figure 3. (a) UV–vis spectra of the nanoplatelet/[C₄mim]Cl solution being tip sonicated for 4, 8, 10, 15, and 20 min, respectively. (b) Detailed view of the peak at ~ 330 nm. (c) Representative AFM image of the Bi₂Te₃ nanoplatelets after 20 min of sonication. (d) UV–vis spectra of the dispersion after 1, 3, 7, 15, and 30 days, respectively. (Inset: photographs showing the solution color change over the course of 30 days.)

Information). The distinct peak could be attributed to the IL solvation layers formed on the Bi₂Te₃ surfaces. The XRD spectra of the as-sonicated sample are the same as the ones before sonication, which confirmed that the final product is still crystallized Bi₂Te₃. Figure 3c is the representative AFM topographical image showing the thicknesses of the exfoliated 2D nanosheets. The overall thickness after the sonication is 15 ± 8 nm. It should be noted that the thickness of as-synthesized nanoplatelets of 1 to 2 μm in diameter is usually ~ 55 nm.²⁶

Because Bi₂Te₃/IL interfaces were ubiquitous in this sonicated Bi₂Te₃/IL sample, as evidenced by the increase in the UV–vis response, and the thicknesses were clearly reduced, we conclude that a significant amount of exfoliation had occurred within the [C₄mim]Cl solvent. To further test the nanosheet dispersion stability, the sonicated sample was observed by UV–vis absorption over the course of 30 days, as presented in Figure 3d. Strikingly, the color of the dispersion remained black over 30 days (consistent with the UV–vis absorption data), indicating a very stable dispersion in comparison to the sonicated Bi₂Te₃/water solution that took only a few hours for complete precipitation. The stable dispersion implies that the IL solvation layers are very robust, prompting a more fundamental analysis of the molecular-level interactions in this system, as discussed in the following sections.

4.2. Exfoliation Mechanism and Kinetics. During the molecular dynamics simulations, we found that the Bi₂Te₃ layers spontaneously separate and are dispersed by the IL. This occurs on a reasonably short time scale, with no artificial pulling or steered molecular dynamics. By observing the simulation trajectories, we found that the exfoliation is initiated by the relative translation of adjacent layers of Bi₂Te₃, which is then followed by layer peeling. This sliding motion results in the exposure of the Te-terminated surface of the material, which is rapidly solvated by the [C₄mim]⁺ component of the IL. Thus, this sliding motion is hypothesized to primarily be the result of attractive electrostatic interactions between the Te surface atoms and the cation. This cation-initiated exfoliation is

identified over the entire range of temperatures that we explored.

To illustrate the exfoliation process, MD simulation snapshots during a representative time window at 550 K are shown in Figure 4. For clarity, only the interfacial tellurium atoms that

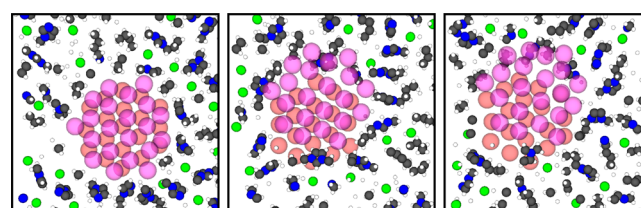


Figure 4. Representative simulation snapshots of the initial stages of exfoliation at 550 K. Only the interfacial Te atoms of one of the van der Waals gaps are shown, along with the [C₄mim]⁺ and Cl[−] species that are located within the horizontal plane of the gap. In the figure, white = H, gray = C, blue = N, and green = Cl. The Te atoms are represented by partially transparent red spheres (bottom) and purple spheres (top). The figures correspond (left to right) to times of 0.0, 0.5, and 0.6 ns.

form the van der Waals gap are included, as well as the IL molecules that are located within the plane of the gap. The intent is to isolate and illustrate the IL molecules that are directly participating in the exfoliation process. The separation is initiated by sliding between two layers, resulting in increased tellurium-terminated edge exposure. The newly exposed edge rapidly adsorbs [C₄mim]⁺ cations (mainly via the imidazolium ring), which exert electrostatic attractive forces on the edge. It is hypothesized that these attractive forces continue to exert stress on the QL, resulting in increasing edge exposure, increased interfacial interactions with the IL, and decreased interaction with the adjacent layers. Once the edge is significantly exposed, the solvation interactions with the IL dominate the interlayer surface energy between adjacent QLs, resulting in conditions favorable to full separation and dispersion. During this sequence of events, the Cl[−] species is not found to participate, at least not in any direct way. By

analyzing the time windows corresponding to the layer separation, this exfoliation mechanism is found to be repeatable.

Although the $[C_4mim]^+$ cation is bulkier than the Cl^- anion, the high selectivity for the cation is explained by the strongly negative electrostatic potential within the van der Waals gap. To illustrate this, an electrostatic potential map of a cross section of the Bi_2Te_3 model in a plane perpendicular to the plane of the van der Waals gap is shown in Figure 5. This

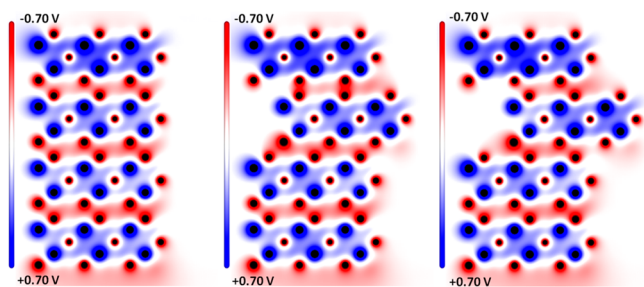


Figure 5. Spatial distribution of the electrostatic potential in a 2D cross-section through a stack of Bi_2Te_3 quintuple layers. The middle and right structures illustrate the change in the electrostatic potential when a layer is shifted by 0.5 and 0.75 nm, respectively.

corresponds to the Bi_2Te_3 model in vacuum, but these same electrostatic features will be present in the solvated system because the atomic charges are held fixed. Although the Bi_2Te_3 quintuple sheets are charge neutral, the partial charge from the tellurium-terminated layers gives rise to a strong electrostatic potential within the van der Waals gap, which attracts $[C_4mim]^+$ and repels the Cl^- species. As these layers are shifted (Figure 5, middle and right), the layers become more susceptible to attack and passivation by the cation species. In an actual experimental sample, it is expected that many of the Bi_2Te_3 edges would naturally protrude (due to sample heterogeneity), and this edge exposure is expected to be critical to the exfoliation.

Our MD analysis of the Bi_2Te_3 exfoliation mechanism suggests that the electrostatic nature of the cation plays a dominant role. This is a consistent observation over a range of temperatures for each layer separated. Although the Cl^- species are less bulky, they are merely spectators during the exfoliation process (Figure 4). In the future, a range of different cations could be evaluated in order to identify any subtle structural influences on the exfoliation process. Moreover, the electrostatic driving forces for IL-assisted exfoliation are also expected to be important for separating other layered dichalcogenide species due to the presence of partial charges in these systems.

Because of the short time scale of the spontaneous Bi_2Te_3 exfoliation in the IL, we were able to directly analyze the kinetics of the exfoliation process. To aid in quantifying the extent of layer separation, a graph of the total Bi_2Te_3 surface area versus time elapsed was plotted for each simulation run. Because of the sliding mechanism of separation, the increase in surface area is relatively gradual, as shown in Figure 6. This is in contrast to discrete exfoliation transitions in which the layers separate in a direction normal to the plane of the nanosheets (without significant interlayer shifting).

As expected, the exfoliation kinetics were strongly dependent on temperature over the temperature interval of 350 to 650 K, and once separated, the layers remained dispersed. Figure 6 shows that the rate of increase in surface area with time is

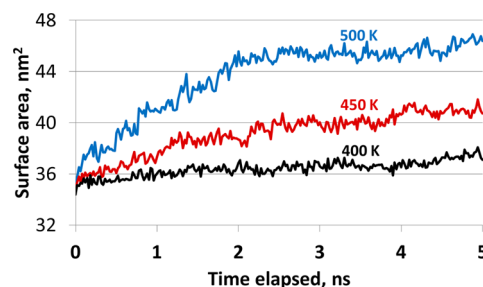


Figure 6. Plot of surface area versus time, illustrating the surface area change with layer exfoliation at 400, 450, and 500 K (higher temperatures omitted for clarity).

greater in the earlier part of the simulation and decreases later in the simulation. This may be explained by the presence of induced solvation layer formation in the IL. For instance, after the first Bi_2Te_3 layer separation, the recently exfoliated layer is still in close proximity to the remaining layers. This exfoliated layer influences the local IL structure, which extends to the neighboring layers. The presence of additional ordered solvation layers near the remaining stacked layers of Bi_2Te_3 results in an increased stability of stacking and more resistance to the next exfoliation event. The gradual exfoliation process is also observed in our experiments (Figure 7). Although the time scales in the MD simulations and the experiments are much different, the overall system dynamics appear to demonstrate similar features.

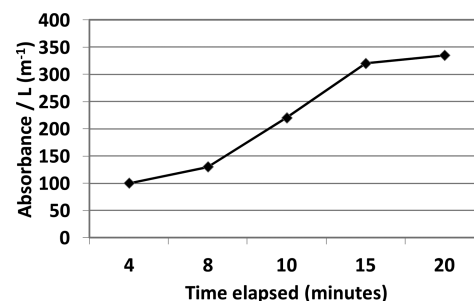


Figure 7. Experimental absorbance at 700 nm versus time elapsed during tip sonication (corresponding to data in Figure 3).

4.3. Solvation Layer Structure. To characterize the Bi_2Te_3 –IL interface, we calculated the linear density profiles of the $[C_4mim]^+$ and Cl^- species perpendicular to the Bi_2Te_3 surfaces. To obtain the linear density profiles, only the density profile within a cylindrical region directly perpendicular to the Bi_2Te_3 surface was analyzed. This cylindrical region was determined by approximating the tellurium surface of the outermost Bi_2Te_3 nanosheet as a circle, which was taken to be the base of the right cylinder. This cylinder was extended in the direction of the IL phase, allowing the collection of data about the structure of the IL layers near the Bi_2Te_3 interfacial region. In this analysis of the IL structure, only the results at 450 K are reported because of the slow convergence at lower temperatures. The viscosities of ILs are typically approximately 2 orders of magnitude greater than those of common organic solvents.⁵¹ This high viscosity (and corresponding low diffusion rate)⁵³ necessitated long simulation times (50 ns of simulation time was used) to gather adequate data for the analysis of the structure of the interfacial layers. It has been previously reported that the prediction of transport properties of ILs

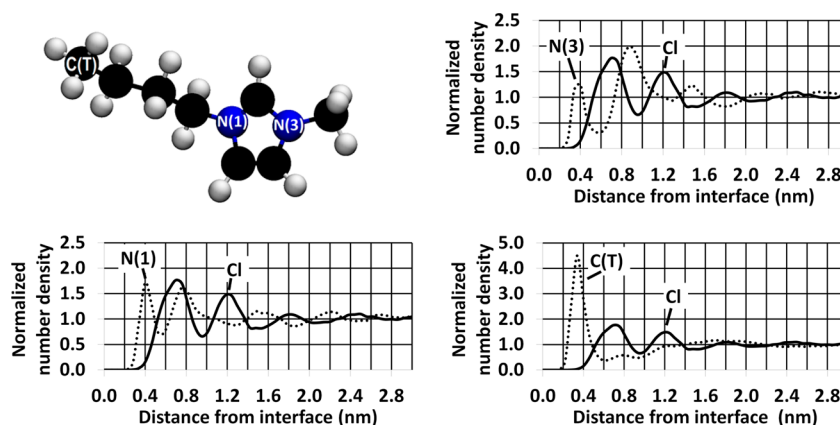


Figure 8. (Top left) Atom site labels for selected atoms of the $[\text{C}_4\text{mim}]^+$ cation model. (Top right, bottom left and right) Density profiles of different IL sites within the Bi_2Te_3 interfacial region at a temperature of 450 K. The horizontal coordinate of the graph represents the orthogonal distance from the plane containing the surface of the Bi_2Te_3 nanosheet.

below 400 K using molecular dynamics requires simulation times of over 100 ns to converge.⁵³ The simulation temperature of 450 K, which is significantly higher than room temperature, was chosen in order to allow for adequate data collection (due to improved IL mobility). By performing further simulations at higher temperatures, we found that the structure of the IL is relatively insensitive to the temperature (Supporting Information, Figure S-2). For instance, at a temperature of 550 K, the general liquid structure is essentially identical, except that the peak heights are lowered by approximately 15–20% and the peak positions are increased by 5%.

The structure of the solvation layers was characterized by calculating the density profiles of both the $[\text{C}_4\text{mim}]^+$ cation and the Cl^- anion in the system. Several different atom centers (corresponding to the labels in Figure 8a) on the $[\text{C}_4\text{mim}]^+$ cation were selected and traced in order to more completely analyze the layer structures, allowing more detailed conclusions to be made about the molecular orientation and specific atomic-level ordering with the solvation layers. The results are illustrated in Figure 8.

The ordered structure of the solvation layers is clearly seen in Figure 8, and the layers propagate 2 to 3 nm away from the surface. The exact position of the surface is defined by the atom centers of the Te atoms, which does not take into account their atomic radii. One of the most notable features is that there is a clear double-layer structure near the Bi_2Te_3 surface, with the first layer composed primarily of the $[\text{C}_4\text{mim}]^+$ cation and the second layer composed of Cl^- (which is strongly excluded from the first layer near the interface). The high density of $[\text{C}_4\text{mim}]^+$ near the surface is presumed to be due to the Coulombic interaction with the Te surface atoms, which have a partial negative charge (as previously illustrated in Figure 5). Even after the first and second layers near the surface, there is still a clear alternating pattern of cations and anions deeper into the bulk liquid. This ionic liquid double-layer structure is very similar to that of another ionic liquid ($[\text{C}_9\text{mim}][\text{Tf}_2\text{N}]$) found near charged graphene surfaces.⁵⁴ Although our systems are charge-neutral, the electrostatic potential near the Te surfaces are within the same range of the charged graphene surfaces (1.0 to -0.4 eV). Other simulation studies of ionic liquids near charged surfaces (mica⁵⁵ and quartz⁵⁶) show similar interfacial ordering behavior.

From the peaks of the N(1) and N(3) sites compared to the peak of the C(T) site, the general configuration and orientation

of the $[\text{C}_4\text{mim}]^+$ species can be distinguished. There is a very large C(T) peak at approximately 0.35 nm, while the N(3) displays peaks near 0.38 and 0.87 nm, with the larger peak at 0.87 nm. The N(1) peak positions are similarly located at 0.40 and 0.80 nm, but the two peak heights are more evenly balanced. Overall, these features indicate that the $[\text{C}_4\text{mim}]^+$ alkane tail is strongly associated with the Bi_2Te_3 surface (first layer), while the imidazolium headgroups are found to be more evenly distributed between the first and second layers. Furthermore, the imidazolium headgroups tend to adopt an orientation with the N(1) to N(3) vectors parallel to the Bi_2Te_3 surface. This is due to the fact that the first peaks in the N(1) and N(3) distribution functions are located at almost the exact same position (0.39 to 0.40 nm), indicating that these sites lie in the same plane (parallel to the surface). The second N(1) and N(3) peaks are located at a distance of 0.40 to 0.45 nm beyond the first peaks, indicating that the second peaks correspond to distinctly different molecules (versus a perpendicular configuration) because the intramolecular N(1) to N(3) distance is approximately 0.21 nm.

The very high ionic strength of the IL results in a solvation structure that is qualitatively different from that seen in conventional solvents. The IL effectively screens the electrostatic interactions between solvated nanosheets and thus forms a “protective layer” surrounding the nanosheets.⁵⁷ The stability of nanosheets in this solution is therefore dependent on strong solvation forces induced by the interfacial layer structure. This ordered structure therefore partially explains the experimentally observed high stability of the exfoliated nanosheets in IL solution.

These linear density profiles can be used to compare the results of our simulations to experimental data. In particular, atomic force microscopy (AFM) can be used to probe the solvation layers under various conditions. Data from force-distance scans can experimentally reveal intermolecular interactions and structure near the IL– Bi_2Te_3 interface, enabling comparisons with our simulations. Experimental AFM studies have been carried out for similar ILs in various systems such as near mica or silica surfaces,^{58,59} indicating that the cation forms a surface solvation layer approximately 0.25 nm from the silica surface. Our results show peaks at 0.35 to 0.40 nm from the Bi_2Te_3 surface for the cation. Because our surface is defined by the atom centers and experimental measurements are defined with respect to the atomic radii, the

experimental value must be corrected by adding a van der Waals atomic radius (the surface of silica is primarily hydroxyl groups, and the van der Waals radius of an oxygen atom is approximately 0.15 nm).⁶⁰ This results in an experimental solvation-layer distance of $(0.25 + 0.15) \text{ nm} = 0.40 \text{ nm}$ from the silica surface atom centers, which is consistent with our simulation values.

5. CONCLUSIONS

The experimental exfoliation of Bi_2Te_3 was successfully demonstrated using a $[\text{C}_4\text{mim}]\text{Cl}$ IL solvent. To gain insights into the mechanism of exfoliation, MD simulations were used to model the exfoliation of Bi_2Te_3 in $[\text{C}_4\text{mim}]\text{Cl}$. The individual quintuple layers of Bi_2Te_3 were rapidly exfoliated and dispersed in our simulation model, allowing an analysis of the kinetics and mechanistic behavior of the process. The structure of the IL solvation layers was characterized and found to contain strongly ordered oscillations that alternate in charge every other layer from cation-rich to anion-rich, explaining the experimentally observed stable dispersion of Bi_2Te_3 nanoplatelets. Furthermore, the apparent solvation layer structure is comparable to previously reported experimental and simulation results from similar systems. We have also determined that the exfoliation process is initiated by the attack of Bi_2Te_3 by the $[\text{C}_4\text{mim}]^+$ cation, and this behavior is consistent with the strongly negative electrostatic potential that exists within the Bi_2Te_3 van der Waals gap. This, coupled with the observation that the first interfacial layer in particular is exceedingly rich in the cation, indicates that the structure and behavior of the cation (here, specifically $[\text{C}_4\text{mim}]^+$) are dominant factor in the intercalation and exfoliation of Bi_2Te_3 nanoplatelets.

In this study, we used a force field for the $\text{Bi}_2\text{Te}_3/\text{IL}$ system that has not previously been used to model the interaction of Bi_2Te_3 with ionic liquid species. Additional benchmarking and/or refinement of the interaction parameters can potentially improve the quantitative accuracy of the interfacial phenomena in these systems. For instance, an experimental comparison of different ionic liquid contact angles on the Bi_2Te_3 surface and the solid–liquid surface energies would provide valuable information for further model refinement. While we have specifically focused on the $\text{Bi}_2\text{Te}_3/[\text{C}_4\text{mim}]\text{Cl}$ system, our analyses should be extensible to the exfoliation of other transitional-metal dichalcogenides, leading to improved solvents for the effective production of 2D materials.

■ ASSOCIATED CONTENT

Supporting Information

Additional UV–vis control sample data. Linear density profiles of the solvent structure at 450 and 550 K. Intermolecular potential parameters used in the MD simulations. Details of the surface-energy calculations. This material is available free of charge via the Internet at <http://pubs.acs.org>.

■ AUTHOR INFORMATION

Corresponding Author

*E-mail: hturner@eng.ua.edu. Tel: 205-348-1733.

Notes

The authors declare no competing financial interest.

■ ACKNOWLEDGMENTS

L.G. acknowledges support from a UA MINT graduate student scholarship (2013 and 2014). H.Q. acknowledges support from

the China Scholarship Council (file no. 2011663055). Partial financial support was provided by the National Science Foundation (EEC-1062705, EEC-1358750).

■ REFERENCES

- (1) Zhang, H. J.; Liu, C. X.; Qi, X. L.; Dai, X.; Fang, Z.; Zhang, S. C. Topological insulators in Bi_2Se_3 , Bi_2Te_3 and Sb_2Te_3 with a single Dirac cone on the surface. *Nat. Phys.* **2009**, *5*, 438–442.
- (2) Peng, H. L.; Lai, K. J.; Kong, D. S.; Meister, S.; Chen, Y. L.; Qi, X. L.; Zhang, S. C.; Shen, Z. X.; Cui, Y. Aharonov-Bohm interference in topological insulator nanoribbons. *Nat. Mater.* **2010**, *9*, 225–229.
- (3) Takahashi, R.; Murakami, S. Thermoelectric transport in topological insulators. *Semicond. Sci. Technol.* **2012**, *27*, 124005.
- (4) Ghaemi, P.; Mong, R. S. K.; Moore, J. E. In-plane transport and enhanced thermoelectric performance in thin films of the topological insulators Bi_2Te_3 and Bi_2Se_3 . *Phys. Rev. Lett.* **2010**, *105*, 166603.
- (5) Kong, D. S.; Dang, W. H.; Cha, J. J.; Li, H.; Meister, S.; Peng, H. L.; Liu, Z. F.; Cui, Y. Few-layer nanoplates of Bi_2Se_3 and Bi_2Te_3 with highly tunable chemical potential. *Nano Lett.* **2010**, *10*, 2245–2250.
- (6) Zhao, Y.; Hughes, R. W.; Su, Z.; Zhou, W.; Gregory, D. H. One-step synthesis of bismuth telluride nanosheets of a few quintuple layers in thickness. *Angew. Chem., Int. Ed.* **2011**, *50*, 10397–10401.
- (7) Wang, D.; Yu, D.; Mo, M.; Liu, X.; Qian, Y. Preparation and characterization of wire-like Sb_2Se_3 and flake-like Bi_2Se_3 nanocrystals. *J. Cryst. Growth* **2003**, *253*, 445–451.
- (8) Wang, W.; Poudel, B.; Yang, J.; Wang, D. Z.; Ren, Z. F. High-yield synthesis of single-crystalline antimony telluride hexagonal nanoplates using a solvothermal approach. *J. Am. Chem. Soc.* **2005**, *127*, 13792–13793.
- (9) Liu, N.; Luo, F.; Wu, H.; Liu, Y.; Zhang, C.; Chen, J. One-step ionic-liquid-assisted electrochemical synthesis of ionic-liquid-functionalized graphene sheets directly from graphite. *Adv. Funct. Mater.* **2008**, *18*, 1518–1525.
- (10) Smith, R. J.; King, P. J.; Lotya, M.; Wirtz, C.; Khan, U.; De, S.; O'Neill, A.; Duesberg, G. S.; Grunlan, J. C.; Moriarty, G.; Chen, J.; Wang, J.; Minett, A. I.; Nicolosi, V.; Coleman, J. N. Large-scale exfoliation of inorganic layered compounds in aqueous surfactant solutions. *Adv. Mater.* **2011**, *23*, 3944–3948.
- (11) Hong, S. S.; Kundhikanjana, W.; Cha, J. J.; Lai, K.; Kong, D.; Meister, S.; Kelly, M. A.; Shen, Z.-X.; Cui, Y. Ultrathin topological insulator Bi_2Se_3 nanoribbons exfoliated by atomic force microscopy. *Nano Lett.* **2010**, *10*, 3118–3122.
- (12) Sutto, T. E.; Duncan, T. T. The intercalation behavior of ionic liquids in the layered metal dichalcogenide TiS_2 . *Electrochim. Acta* **2012**, *77*, 204–211.
- (13) Seddon, K. R. Ionic liquids for clean technology. *J. Chem. Technol. Biotechnol.* **1997**, *68*, 351–356.
- (14) Wasserscheid, P.; Keim, W. Ionic liquids—new “solutions” for transition metal catalysis. *Angew. Chem., Int. Ed.* **2000**, *39*, 3772–3789.
- (15) Wilkes, J. S. A short history of ionic liquids—from molten salts to neoteric solvents. *Green Chem.* **2002**, *4*, 73–80.
- (16) Bates, E. D.; Mayton, R. D.; Ntai, I.; Davis, J. H. CO_2 capture by a task-specific ionic liquid. *J. Am. Chem. Soc.* **2002**, *124*, 926–927.
- (17) Cadena, C.; Anthony, J. L.; Shah, J. K.; Morrow, T. I.; Brennecke, J. F.; Maginn, E. J. Why is CO_2 so soluble in imidazolium-based ionic liquids? *J. Am. Chem. Soc.* **2004**, *126*, 5300–5308.
- (18) Capello, C.; Fischer, U.; Hungerbühler, K. What is a green solvent? A comprehensive framework for the environmental assessment of solvents. *Green Chem.* **2007**, *9*, 927–934.
- (19) Dilip, M. Cradle to grave: How green are ionic liquids? *Nanomater. Energy* **2012**, *1*, 193–206.
- (20) Canongia Lopes, J. N.; Deschamps, J.; Pádua, A. A. H. Modeling Ionic Liquids Using a Systematic All-Atom Force Field. *J. Phys. Chem. B* **2004**, *108*, 2038–2047.
- (21) Shah, J. K.; Brennecke, J. F.; Maginn, E. J. Thermodynamic properties of the ionic liquid 1-n-butyl-3-methylimidazolium hexafluorophosphate from Monte Carlo simulations. *Green Chem.* **2002**, *4*, 112–118.

- (22) Kamath, G.; Baker, G. A. In silico free energy predictions for ionic liquid-assisted exfoliation of a graphene bilayer into individual graphene nanosheets. *Phys. Chem. Chem. Phys.* **2012**, *14*, 7929–7933.
- (23) Kamath, G.; Baker, G. A. Are ionic liquids suitable media for boron nitride exfoliation and dispersion? Insight via molecular dynamics. *RSC Adv.* **2013**, *3*, 8197–8202.
- (24) Rathod, N.; Hatzikiriakos, S. G. The effect of surface energy of boron nitride on polymer processability. *Polym. Eng. Sci.* **2004**, *44*, 1543–1550.
- (25) Wang, S.; Zhang, Y.; Abidi, N.; Cabrales, L. Wettability and Surface Free Energy of Graphene Films. *Langmuir* **2009**, *25*, 11078–11081.
- (26) Guo, L.; Aglan, A.; Quan, H.; Sun, J.; Tang, C.; Song, J.; Szulczewski, G.; Wang, H.-T. Selective adsorption of bismuth telluride nanoplatelets through electrostatic attraction. *Phys. Chem. Chem. Phys.* **2014**, *16*, 11297–11302.
- (27) Zhang, G. Q.; Wang, W.; Lu, X. L.; Li, X. G. Solvothermal synthesis of V-VI binary and ternary hexagonal platelets: The oriented attachment mechanism. *Cryst. Growth Des.* **2009**, *9*, 145–150.
- (28) Hess, B.; Kutzner, C.; van der Spoel, D.; Lindahl, E. GROMACS 4: Algorithms for Highly Efficient, Load-Balanced, and Scalable Molecular Simulation. *J. Chem. Theory Comput.* **2008**, *4*, 435–447.
- (29) Jorgensen, W. L.; Maxwell, D. S.; Tirado-Rives, J. Development and Testing of the OPLS All-Atom Force Field on Conformational Energetics and Properties of Organic Liquids. *J. Am. Chem. Soc.* **1996**, *118*, 11225–11236.
- (30) Essmann, U.; Perera, L.; Berkowitz, M. L.; Darden, T.; Lee, H.; Pedersen, L. G. A smooth particle mesh Ewald method. *J. Chem. Phys.* **1995**, *103*, 8577–8592.
- (31) Zhao, Y.; Liu, X.; Lu, X.; Zhang, S.; Wang, J.; Wang, H.; Gurau, G.; Rogers, R. D.; Su, L.; Li, H. The Behavior of Ionic Liquids under High Pressure: A Molecular Dynamics Simulation. *J. Phys. Chem. B* **2012**, *116*, 10876–10884.
- (32) Liu, H.; Zhang, Z.; Bara, J. E.; Turner, C. H. Electrostatic Potential within the Free Volume Space of Imidazole-Based Solvents: Insights into Gas Absorption Selectivity. *J. Phys. Chem. B* **2014**, *118*, 255–264.
- (33) Turner, C. H.; Cooper, A.; Zhang, Z.; Shannon, M. S.; Bara, J. E. Molecular Simulation of the Thermophysical Properties of N-Functionalized Alkylimidazoles. *J. Phys. Chem. B* **2012**, *116*, 6529–6535.
- (34) Qiu, B.; Ruan, X. L. Molecular dynamics simulations of lattice thermal conductivity of bismuth telluride using two-body interatomic potentials. *Phys. Rev. B* **2009**, *80*, 165203.
- (35) Huang, B. L.; Kaviani, M. Ab initio and molecular dynamics predictions for electron and phonon transport in bismuth telluride. *Phys. Rev. B* **2008**, *77*, 125209.
- (36) Qiu, B.; Ruan, X. L. Thermal conductivity prediction and analysis of few-quintuple Bi₂Te₃ thin films: A molecular dynamics study. *Appl. Phys. Lett.* **2010**, *97*, 183107.
- (37) Qiu, B.; Sun, L.; Ruan, X. L. Lattice thermal conductivity reduction in Bi₂Te₃ quantum wires with smooth and rough surfaces: A molecular dynamics study. *Phys. Rev. B* **2011**, *83*, 035312.
- (38) Wang, Y.; Xu, X. Molecular dynamics studies of ultrafast laser-induced nonthermal melting. *Appl. Phys. A* **2013**, *110*, 617–621.
- (39) Kullmann, W.; Eichhorn, G.; Rauh, H.; Geick, R.; Eckold, G.; Steigenberger, U. Lattice-dynamics and phonon-dispersion in the narrow gap semiconductor Bi₂Te₃ with sandwich structure. *Phys. Status Solidi B* **1990**, *162*, 125–140.
- (40) Rappe, A. K.; Casewit, C. J.; Colwell, K. S.; Goddard, W. A.; Skiff, W. M. UFF, a full periodic-table force-field for molecular mechanics and molecular-dynamics simulations. *J. Am. Chem. Soc.* **1992**, *114*, 10024–10035.
- (41) Parrinello, M.; Rahman, A. Crystal Structure and Pair Potentials: A Molecular-Dynamics Study. *Phys. Rev. Lett.* **1980**, *45*, 1196–1199.
- (42) Parrinello, M.; Rahman, A. Polymorphic transitions in single crystals: A new molecular dynamics method. *J. Appl. Phys.* **1981**, *52*, 7182–7190.
- (43) Hoover, W. G. Canonical dynamics: Equilibrium phase-space distributions. *Phys. Rev. A* **1985**, *31*, 1695–1697.
- (44) Nakajima, S. The crystal structure of Bi₂Te₃-xSex. *J. Phys. Chem. Solids* **1963**, *24*, 479–485.
- (45) Hao, G.; Qi, X.; Yang, L.; Liu, Y.; Li, J.; Ren, L.; Sun, F.; Zhong, J. Growth and surface potential characterization of Bi₂Te₃ nanoplates. *AIP Adv.* **2012**, *2*, 012114–012118.
- (46) Guo, L.; Ivey, B. C.; Aglan, A.; Tang, C.; Song, J.; Turner, C. H.; Frazier, R. M.; Gupta, A.; Wang, H.-T. Vapor phase growth of bismuth telluride nanoplatelets on flexible polyimide films. *ECS Solid State Lett.* **2013**, *2*, P19–P21.
- (47) Barnes, J. O.; Rayne, J. A.; Ure, R. W. Lattice expansion of Bi₂Te₃ from 4.2K to 600K. *Phys. Lett. A* **1974**, *46*, 317–318.
- (48) Jin, J.; Miller, J. D.; Dang, L. X. Molecular dynamics simulation and analysis of interfacial water at selected sulfide mineral surfaces under anaerobic conditions. *Int. J. Miner. Process.* **2014**, *128*, 55–67.
- (49) Varshney, V.; Patnaik, S. S.; Muratore, C.; Roy, A. K.; Voevodin, A. A.; Farmer, B. L. MD simulations of molybdenum disulphide (MoS₂): Force-field parameterization and thermal transport behavior. *Comput. Mater. Sci.* **2010**, *48*, 101–108.
- (50) Holbrey, J. D.; Reichert, W. M.; Nieuwenhuyzen, M.; Johnson, S.; Seddon, K. R.; Rogers, R. D. Crystal polymorphism in 1-butyl-3-methylimidazolium halides: supporting ionic liquid formation by inhibition of crystallization. *Chem. Commun.* **2003**, 1636–1637.
- (51) Huddleston, J. G.; Visser, A. E.; Reichert, W. M.; Willauer, H. D.; Broker, G. A.; Rogers, R. D. Characterization and comparison of hydrophilic and hydrophobic room temperature ionic liquids incorporating the imidazolium cation. *Green Chem.* **2001**, *3*, 156–164.
- (52) Fredlake, C. P.; Crosthwaite, J. M.; Hert, D. G.; Aki, S. N. V. K.; Brennecke, J. F. Thermophysical Properties of Imidazolium-Based Ionic Liquids. *J. Chem. Eng. Data* **2004**, *49*, 954–964.
- (53) Andreussi, O.; Marzari, N. Transport properties of room-temperature ionic liquids from classical molecular dynamics. *J. Chem. Phys.* **2012**, *137*, 044508.
- (54) Uysal, A.; Zhou, H.; Feng, G.; Lee, S. S.; Li, S.; Fenter, P.; Cummings, P. T.; Fulvio, P. F.; Dai, S.; McDonough, J. K.; Gogotsi, Y. Structural Origins of Potential Dependent Hysteresis at the Electrified Graphene/Ionic Liquid Interface. *J. Phys. Chem. C* **2014**, *118*, S69–S74.
- (55) Payal, R. S.; Balasubramanian, S. Effect of cation symmetry on the organization of ionic liquids near a charged mica surface. *J. Phys.: Condens. Matter* **2014**, *26*, 284101.
- (56) Wang, Y. L.; Laaksonen, A. Interfacial structure and orientation of confined ionic liquids on charged quartz surfaces. *Phys. Chem. Chem. Phys.* **2014**, *16*, 23329–23339.
- (57) Hayes, R.; Warr, G. G.; Atkin, R. At the interface: solvation and designing ionic liquids. *Phys. Chem. Chem. Phys.* **2010**, *12*, 1709–1723.
- (58) Atkin, R.; Warr, G. G. Structure in confined room-temperature ionic liquids. *J. Phys. Chem. C* **2007**, *111*, S162–S168.
- (59) Hayes, R.; El Abedin, S. Z.; Atkin, R. Pronounced structure in confined aprotic room-temperature ionic liquids. *J. Phys. Chem. B* **2009**, *113*, 7049–7052.
- (60) Bondi, A. van der Waals Volumes and Radii. *J. Phys. Chem.* **1964**, *68*, 441–451.